Bifunctional and Self-Supported NiFeP-Layer-Coated NiP Rods for Electrochemical Water Splitting in Alkaline Solution

Diao, Fangyuan; Huang, Wei; Ctistis, Georgios; Wackerbarth, Hainer; Yang, Yuan; Si, Pengchao; Zhang, Jingdong; Xiao, Xinxin; Engelbrekt, Christian

Published in:
ACS Applied Materials and Interfaces

Link to article, DOI:
10.1021/acsami.1c03089

Publication date:
2021

Document Version
Peer reviewed version

Cite this paper: https://doi.org/10.1021/acsami.1c03089

Bifunctional and Self-supported NiFeP Layer Coated NiP Rods for Electrochemical Water Splitting in Alkaline Solution

Fangyuan Diao[1], Wei Huang[1], Georgios Ctistis[2], Hainer Wackerbarth[2], Yuan Yang[3], Pengchao Si[3], Jingdong Zhang[1], Xinxin Xiao[1], Christian Engelbrekt[1]**

[1] Department of Chemistry, Technical University of Denmark, DK-2800 Kongens Lyngby, Denmark.

[2] Institut für Nanophotonik Göttingen e.V., Department of Photonic Sensor Technology, Hans-Adolf-Krebs-Weg 1, 37077 Göttingen, Germany

[3] Key Laboratory for Liquid-Solid Structural Evolution and Processing of Materials (Ministry of Education), Research Center for Carbon Nanomaterials, School of Materials Science and Engineering, Shandong University, Jinan 250061, P. R.

KEYWORDS

Nickel iron phosphides; Prussian blue analogue derivative; Core-shell structure; Overall water splitting; Excellent stability

ABSTRACT

Designing efficient and robust non-precious metal based electrocatalysts for overall water electrolysis, which is mainly limited by the oxygen evolution reaction (OER), for hydrogen production remains a major challenge for the hydrogen economy. In this work, a bimetallic NiFeP catalyst is coated on nickel phosphide rods grown on nickel foam (NiFeP@NiP@NF). This self-supported and interfacially connected electrode structure is favorable for mass transfer and reducing electrical resistance during electrocatalysis. The preparation of NiFeP@NiP@NF is optimized in terms of i) the coprecipitation time of the NiFe Prussian blue analogue layer that serves as phosphides precursor and ii) the phosphidation temperature. The optimized sample exhibits excellent OER performance delivering current densities of 10 and 100 mA cm^{-2} at low overpotentials of 227 and 252 mV in 1.0 M KOH, respectively, and maintaining 10 mA cm^{-2} for more than 120 h without obvious degradation. Moreover, it can also be operated as the hydrogen evolution electrocatalyst, requiring an overpotential of 105 mV at 10 mA cm^{-2} in the same medium. Thus, the as-prepared material was tentatively utilized as a bifunctional electrocatalyst in a symmetric electrolyzer, requiring a voltage bias of 1.57 V to afford 10 mA cm^{-2} in 1.0 M KOH, while exhibiting outstanding stability.

1. INTRODUCTION

Hydrogen (H_2) is an ideal energy carrier due to its high specific energy density (more than 120 MJ kg^{-1}) and its oxidation with air only produces non-toxic water.[1–4] Electrochemical water splitting for hydrogen production involves the cathodic hydrogen evolution reaction (HER) and anodic oxygen evolution reaction (OER), and represents a green energy storage platform when using sustainable but intermittent electricity sources like solar and wind.[5] Pt- and Ir (or Ru)-related

materials are the benchmark electrocatalysts for HER and OER, respectively. [6–10] However, their high cost and scarcity in nature pose significant difficulties in large-scale applications.[11–13] Thus, research on well-engineered and efficient electrocatalysts employing high-abundance element as alternatives is attracting increasing attention.[14–16]

Among various non-precious electrocatalysts, transition metal phosphides (TMPs) have emerged as a desirable electrocatalysts towards electrocatalytic water splitting.[17] In the HER process, the metal and phosphorous sites of TMPs can form hydrides and trap protons, respectively, similar to the catalytic mechanisms of hydrogenases.[18,19] Meanwhile, the real catalytic sites for OER are surface metal oxides/hydroxides derived in situ.[20,21] Up to now, TMPs including Mo-,[22–24] Co-,[18,25] Fe-,[26] and Ni-[19,27,28] phosphides have been reported with reasonable activities towards HER in acidic or alkaline solution, with a fair number of them such as Ni- and Co-related metal phosphides[29–32] also showing efficient OER performance. Bimetallic phosphides show better performance than monometallic phosphides due to synergistic effects and modified electronic structures.[28,29] For instance, Yang *et al.* found that Fe-doped Co_2P required a much lower overpotential to reach the same current density compared with Co_2P, $Ni_{12}P_5$, and Fe_2P.[29] Ren *et al.* optimized the performance of FeNiP nanoparticles on carbon sheets towards OER and HER by tuning the ratio of Fe_2P and Ni_2P.[35] However, challenges still remain for obtaining TMP-based bifunctional electrocatalysts with high efficiency and long-term stability for HER and OER in the same electrolyte.[32,36,37] Facile and reproducible methods for scalable production of catalysts are also desired.

In situ preparation of electrocatalysts on conductive substrates, such as nickel foam (NF),[32,38] carbon cloth,[39] and titanium foil,[40] is a practical synthesis route. It not only simplifies the electrode production, but can also lead to reduced contact resistance between catalysts and substrates.[41] NF

is desirable for in situ construction of TMP microstructures as it is cheap, hydrophilic and conducting. Furthermore, its macroporous structure provides open paths for H_2 and oxygen (O_2) liberation during electrolysis. There is a growing number of reports on bifunctional catalysts on NF for HER and OER, which would greatly simplify the catalyst preparation process. For example, Xu *et al.* synthesized three-dimensional porous FeP/Ni_2P hybrids by treating NF with iron nitrate and subsequent phosphidation.[32] Ahn and associates reported porous and carbon-incorporated Ni-Fe-P nanorods on NF derived from Ni-Fe metal-organic frameworks.[38] Both cases achieved a benchmark current density of 10 mA cm^{-2} with a whole cell voltage less than 1.60 V towards water splitting in 1.0 M KOH and good stability. Rationally tailored hierarchical structures of different types of TMPs for better performance remains rarely studied.

In this work, we design a hierarchical structure of nickel and iron phosphide hybrids coated on nickel phosphide rods that have been grown on NF (NiFeP@NiP@NF). The NiFeP is derived from a NiFe Prussian blue analogue (NiFe PBA), which is conveniently formed on nickel phosphate hydrate (NiPO) rods, that are themselves grown on NF (NiFe PBA@NiPO@NF), and subsequently converted to NiP. NiFeP@NiP@NF is successfully synthesized by a reproducible and facile method, and shows excellent activity and outstanding stability towards both OER and HER in 1.0 M KOH. The optimized sample registers low overpotentials of 227 and 105 mV for OER and HER at a current density of 10 mA cm^{-2}, respectively. Moreover, a symmetrical two-electrode alkaline electrolyzer with NiFeP@NiP@NF as both cathode and anode only required 1.57 and 1.64 V to reach 10 and 20 mA cm^{-2}, respectively, outperforming major bifunctional catalysts in literature.

2. RESULTS AND DISCUSSIONS

2.1. Preparation and structural characterization

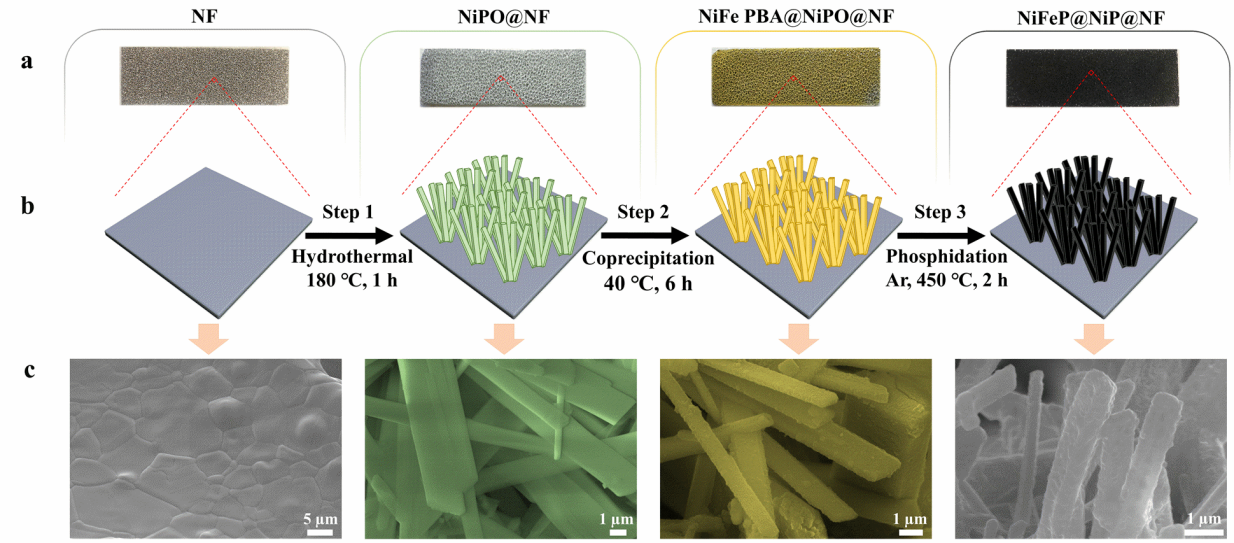

Figure 1. Overview of synthesis procedure. (a) Photographs (width: ~1 cm; length: ~3 cm), (b) synthesis scheme with representative conditions, and (c) false colored SEM images of (left to right) NF, NiPO@NF, NiFe PBA@NiPO@NF and NiFeP@NiP@NF.

The synthesis procedure of NiFeP@NiP@NF involves three steps as shown in **Figure 1**. NF with its macroporous structure (pore size: 277 ± 133 μm, frame width: 64 ± 6 μm), large surface area and good conductivity served as the scaffold for the active catalyst (Figure 1 and Figure S1). In the first step, NiPO rods were constructed on the surface of NF (NiPO@NF) via a hydrothermal method in a microwave synthesizer. Then, a NiFe PBA layer was grown on the NiPO rods through a facile coprecipitation method during which the sample color changed from light green to yellow (Step 2, Figure 1). Finally, NiFe PBA@NiPO@NF was transformed into the black NiFeP@NiP@NF via phosphidation under Ar atmosphere, where NaH_2PO_2 at the upstream releases PH_3 as the phosphorus source (Step 3, Figure 1).[42]

The peaks in the powder X-ray diffraction (XRD) pattern of NiPO@NF in Figure S2 match well with monoclinic $Ni_3(PO_4)_2 \cdot 8H_2O$ (Inorganic Crystal Structure Database Collection Code, ICSD Coll. Code, 240946) and also includes expected peaks from the NF support, indicating that a pure phase of NiPO is obtained in the first step. Energy dispersive spectroscopy (EDS) analysis (Figure S3c) confirms a Ni:P atomic ratio of 3.1:2, consistent with the XRD results and the formula above. The Fourier transform infrared (FT-IR) spectrum of NiPO@NF is shown in Figure S4a. Peaks at 3426, 3139 and 3000 cm^{-1} are assigned to O-H stretching vibrations in water, and at 1587 and 740 cm^{-1} to bending and vibrational modes of water molecules.[43] Bands in the regions of 1100-800 cm^{-1} and 580-540 cm^{-1} are assigned to vibration of PO_4^{3-}.[44,45] Scanning electron microscope (SEM) micrographs in Figure 1c, Figure S3a and S3b show the morphology of NiPO@NF. Small amounts of Ni^{2+} and Fe^{3+} in the solution aid in achieving uniformly distributed and regularly shaped NiPO rods on the NF as seen from the morphology of reference samples made without these additives (Figure S5). The optimized NiPO rods show a prismatic shape with a length of tens of micrometers, a width of 1.51 ± 0.44 μm and smooth surfaces (Figure 1c). This morphology can provide a large surface area and abundant nucleation sites for the growth of NiFe PBA in the following step.

To grow a thin layer of NiFe PBA on the surface of the NiPO rods, coprecipitation of PBA in a solution containing Ni^{2+} and $[Fe(CN)_6]^{3-}$ was carried out. Nickel ions from local dissolution act as nucleation sites to react with $[Fe(CN)_6]^{3-}$, leading to the formation of a NiFe PBA layer along the NiPO rod surface. During growth, nickel ions can be supplemented from bulk solution, resulting in the complete coverage of the rods with NiFe PBA.[46,47] Extending the growth time leads to thicker NiFe PBA layers and the formation of cubic NiFe PBA features. Figure 1c and Figure S6 show the SEM images of NiFe PBA@NiPO@NF obtained with different NiFe PBA growth durations ranging from 1 to 24 h. Characterization with XRD, FT-IR, and X-ray photoelectron

spectroscopy (XPS) was conducted to verify the crystal phase and composition of NiFe PBA@NiPO@NF. Compared to the XRD patterns of NiPO@NF in Figure S7a, several additional peaks appear at 17.57˚, 24.95˚, 35.61˚, and 39.97˚ in the pattern of NiFe PBA@NiPO@NF, ascribed to cubic $KNiFe(CN)_6$ (ICSD Coll. Code: 89338) confirming the formation of PBA.[48,49] This is further supported by the appearance of a peak at 2089 cm^{-1} in the FT-IR spectrum (Figure S4b) and 2100-2200 cm^{-1} in the Raman spectrum (Figure S4) representing the CN group coordinated by Ni and Fe.[50,51] Figure S4g shows the Raman spectrum of NiFe PBA@NiPO@NF between 1900 and 2400 cm^{-1} in which two peaks at 2103 and 2140 cm^{-1} are attributed to CN vibration of Fe^{II}–CN–Ni^{II} and Fe^{II}–CN–Ni^{III}, and another peak at 2174 cm^{-1} is from CN vibration in Fe^{III}–CN–Ni^{II}.[52,53] The surface elemental composition of the NiFe PBA@NiPO@NF is determined through quantification of the high-resolution XPS spectra of K 2p, Ni 2p, Fe 2p and N 1s, showing an atomic K:Ni:Fe:N ratio of approximately 1.03:1.03:1:5.00, in agreement with the expected NiFe PBA composition (Figure S8). SEM images (Figure S7b) indicate that the thickness of the NiFe PBA layer is 120–160 nm. All these results verify that the core-shell structure of the NiFe PBA@NiPO@NF was successfully constructed. In the final step, NiFe PBA@NiPO@NF was calcined together with $NaH_2PO_2 \cdot H_2O$ under Ar atmosphere at 450 ℃ to obtain NiFeP@NiP@NF. During this process, NiFe PBA and NiPO were completely reduced by PH_3 released by decomposition of $NaH_2PO_2 \cdot H_2O$ during the phosphidation step. Peaks in the XRD pattern of NiFeP@NiP@NF in **Figure 2**a are indexed to a mixture of Ni_2P (ICSD Coll. Code: 105306), $Ni_{12}P_5$ (ICSD Coll. Code: 646121), and Fe_2P (ICSD Coll. Code: 70113). SEM images of NiFeP@NiP@NF (Figure 1c and Figure S9) suggests that the rod-like structure is maintained after phosphidation, which is quite different from NiP@NF consisting of deformed and granular rods (Figure S10). Elemental mapping demonstrates a uniform distribution of Ni, Fe, P, and O on the

surface of NiFeP@NiP@NF, proving further that the precursor was transformed into a phosphide composite (Figure 2g-2j). TEM images in Figure S11 also indicate a core-shell structure where the NiP rod is fully covered by a layer of NiFeP with a thickness of approximately of 140 nm (Figure S11c). EDS analyses was carried out at the edge and center of the rod further supports Fe localization in the shell (Figure S11d). In the FT-IR spectrum of NiFeP@NiP@NF, there are no remaining peaks from water and CN vibration, which confirms the conversion of the material during phosphidation (Figure S4c). Besides this, Raman spectra of NiFeP@NiP@NF and NiFeP@NF (prepared by phosphidation of NiFe PBA directly grown on NF) exhibit peaks around 1375 and 1570 cm^{-1} corresponding to the D- and G-band of disordered structure and graphitic sp^2 hybridized carbon materials respectively (Figure S4h).[54] This indicates the formation of graphene-like carbon structures in the PBA-derived NiFeP during phosphidation. Such features were not found for NiP@NF.

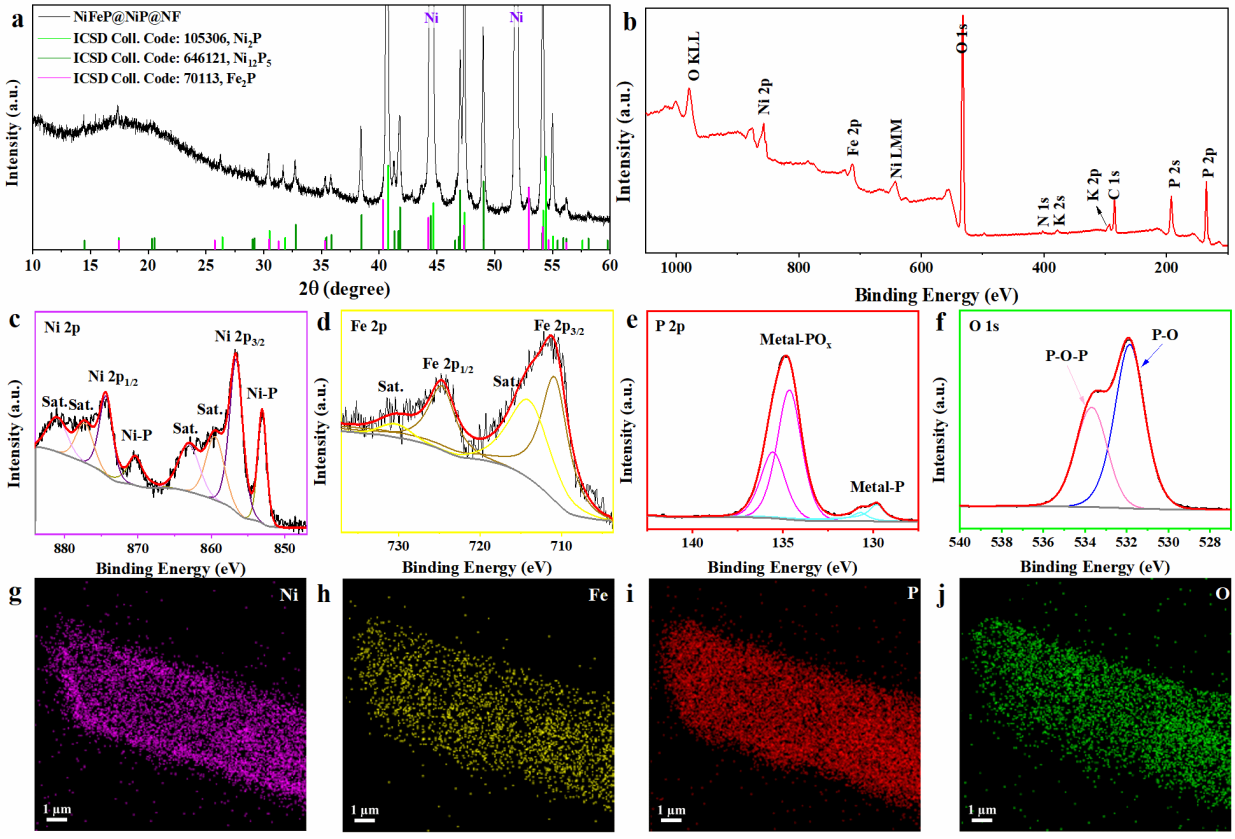

Figure 2. (a) XRD patterns and (b) XPS survey spectrum of NiFeP@NiP@NF. (c-f) High-resolution XPS spectra and (g-j) elemental mapping of elemental Ni, Fe, P and O of NiFeP@NiP@NF, respectively.

The chemical state and composition of the surface of NiFeP@NiP@NF were further disclosed by XPS demonstrating the presence of Ni, Fe, K, C, N, O and P (Figure 2b). The atomic ratio of K:Ni:Fe:P on the surface of NiFeP@NiP@NF is determined to be 0.37:1.4:1:6.5. In comparison to the surface composition of NiFe PBA@NiPO@NF (K:Ni:Fe = 1.03:1.03:1), the relative content of Fe and K reduces for NiFeP@NiP@NF (K:Ni:Fe = 0.37:1.44:1), which is caused by the rearrangement of atoms during phosphidation. The sharp doublet at 853.1/870.3 eV in the high-resolution XPS spectrum of Ni 2p (Figure 2c) is assigned to $Ni^{\delta+}$ ($0 < \delta < 2$) in nickel phosphide species, with a shake-up satellite doublet (marked Sat.) at 859.5/877.3 eV.[55] The binding energy (BE) of $Ni^{\delta+}$ is close to the metallic Ni $2p_{3/2}$ BE of 852.6 eV.[56] The doublet at around 856.6/874.4 eV with a satellite at 863.1/881.0 eV corresponds to Ni^{2+} probably in connection with phosphate arising from surface passivation of the phosphide.[55,57] In the high-resolution XPS spectrum of Fe 2p (Figure 2d), two broad core doublets located at 711.0/724.8 eV and 714.3/730.7 eV are ascribed to the Fe^{3+} in Fe-O-P in iron phosphate formed due to superficial oxidation.[58] The high-resolution spectrum of P 2p in Figure 2e shows a doublet at 129.8/130.7 eV representing P in metal phosphide species with a slightly negatively charged P. The doublet at 134.7/135.6 eV corresponds to P-O in the surface metal phosphates formed due to exposure to air. Moreover, two O 1s peaks at 531.9 eV and 533.7 eV, respectively, correspond to non-bridging oxygen (P-O) and bridging oxygen (P-O-P) species.[58,59] In addition, no characteristic peak of metal oxides are observed at around 530 eV in Figure 2f, which demonstrates that metal ions are bound in phosphides and phosphates.[58–60] During phosphidation at 450 ℃ for 2 h, NiFe PBA decomposed and the CN ligands are removed

from the sample. Some of the CN ligands may be reduced by PH_3, resulting in small amounts of carbon and nitrogen in the NiFeP matrix.[61] As discussed above, carbon element should exist in graphene-like carbon structures, which is consistent with C 1s spectrum analysis in Figure 12a. In Figure S12b, the relatively weak peak around the binding energy of 402 eV represents N 1s, which could be assigned to some oxygenated nitrogen species.[62] This is not from remaining CN as evidenced by the lack of characteristic peaks in the Raman, IR and XPS spectra, although it is difficult to determine the precise chemical nature of the N-dopant.

2.2. Electrochemical catalytic activity

The electrocatalytic OER activity of NiFeP@NiP@NF was investigated using a three-electrode setup in 1.0 M KOH at room temperature (RT). **Figure 3**a displays *iR*-corrected polarization curves of NiFeP@NiP@NF, NiP@NF (prepared by phosphidation of NiPO@NF), NiPO@NF, NiFe PBA@NiPO@NF, RuO_2 paste on NF (RuO_2@NF), and bare NF. NiPO@NF shows much better OER performance than bare NF and RuO_2@NF. With the coating of NiPO@NF by a NiFe PBA layer, the OER performance improves slightly. The phosphidation products, including NiP@NF and NiFeP@NiP@NF, registered the best OER performances. Figure 3b summarizes the observed overpotentials at a current density of 100 and 400 mA cm^{-2} for all samples. NiFeP@NiP@NF requires the lowest η_{100} of 252 mV, which outperforms the RuO_2 on NF (η_{100} = 352 mV) and other related materials in this work including NiFe PBA@NiPO@NF (η_{100} = 310 mV), NiP@NF (η_{100} = 299 mV), NiPO@NF (η_{100} = 326 mV), and NF (η_{100} = 445 mV). The same trend is found for η_{400}. We also explore the OER performance of NiFe PBA grown directly on nickel foam (NiFe PBA@NF, η_{10} = 352 mV), and the corresponding phosphidation material (NiFeP@NF, η_{10} = 262 mV), Figure S14. Furthermore, NiFeP@NiP@NF exhibits an electrocatalytic OER performance comparable to various nonprecious metal phosphides, oxides

and other related electrocatalysts in the literature (Table S1). Figure 3c displays the Tafel behavior of the tested materials, with smaller Tafel slopes indicating more favorable OER kinetics. NiFeP@NiP@NF possesses the smallest Tafel slope of 60.7 mV dec^{-1} and maintains linearity in the higher current density region of the polarization curves, which illustrates fast electron and mass transport between the electrolyte and catalyst.[21] Nyquist plots show that the charge transfer resistance (R_{ct}) of NiFeP@NiP@NF at the potential of 1.5 V is approximately 2.4 Ω, far smaller than those of other samples at the same potential (Figure 3d and Table S4). All the performance metrics, including the η_{100} of 252 mV, Tafel slope of 60.7 mV dec^{-1} and R_{ct} of 2.4 Ω@1.5 V, highlight NiFeP@NiP@NF as the best candidate for OER in terms of reaction kinetics. To further evaluate the application potential of the material, the operational stability of NiFeP@NiP@NF (Figure 3e) studied via multistep chronopotentiometry (CP) tests in the current density range from 10 mA cm^{-2} to 100 mA cm^{-2} and back to 10 mA cm^{-2} (1 h duration for each current density). The overpotential increases with current density (inset of Figure 3e), while no discernable increase of the operational potential when returning to 10 mA cm^{-2} after 6 h test was observed (Figure 3e). This reveals that NiFeP@NiP@NF is capable of functioning over a wide range of current densities with good stability. The long-term operation of NiFeP@NiP@NF over a course of 120 h at 10 mA cm^{-2} barely sees an increase in potential (3 mV), and almost overlapping polarization curves are recorded before and after the stability test (Figure 3f). Further, stability is evaluated at a higher current load of 500 mA cm^{-2} for 30 h leading to a minimal potential increase of just 1 mV, validating that the sample is also very stable at a much larger current density and thus shows robust OER performance (Figure S17).

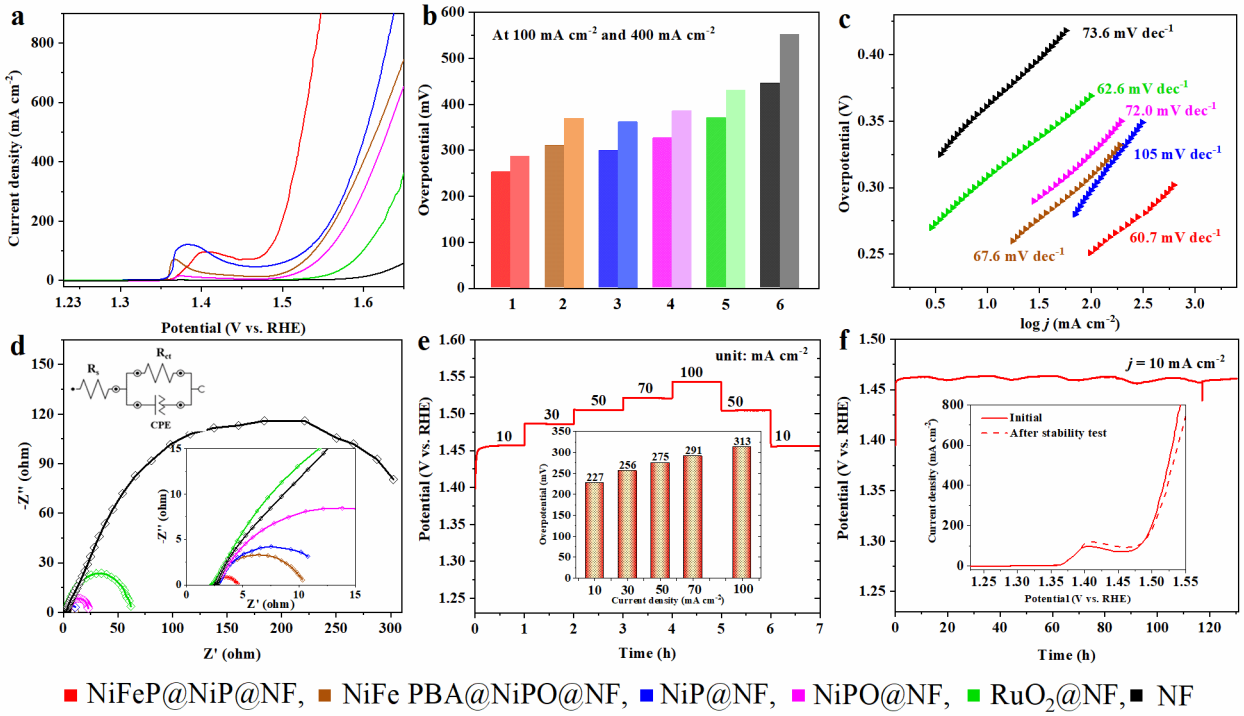

Figure 3. OER performance tests in 1.0 M KOH. (a) *iR*-corrected polarization curves. Scan rate: 2 mV s^{-1}. (b) OER overpotentials at the current density of 100 mA cm^{-2} (left, dark color) and 400 mA cm^{-2} (right, light color). (c) Tafel curves. (d) Nyquist plots. Inset in (d) is the equivalent circuit used to fit the Nyquist plot. (e) CP tests recorded at different current densities from 10 mA cm^{-2} to 100 mA cm^{-2}. The inset shows the corresponding overpotentials at different current densities. (f) Long-term stability test of NiFeP@NiP@NF. Inset: *iR*-corrected polarization curves before and after stability test for 120 h. Scan rate: 2 mV s^{-1}.

The HER performance of NiFeP@NiP@NF has also been evaluated in the same alkaline environment as the previous OER experiments (**Figure 4**). Commercial 20 wt.% platinum on graphitized carbon black pasted on NF (Pt/C@NF) displays excellent HER activity with an onset potential near 0 V, requiring small overpotentials of 21 and 95 mV to drive 10 and 100 mA cm^{-2}, respectively (Figure 4a). NiFeP@NiP@NF also exhibits outstanding electrocatalytic activity

toward HER with an overpotential of 105 mV to yield 10 mA cm^{-2}, lower than those of NiP@NF (η_{10} = 129 mV), NiPO@NF (η_{10} = 148 mV), NiFe PBA@NiPO@NF (η_{10} = 158 mV), and NF (η_{10} = 171 mV) (Figure 4b). To achieve a high current density of 300 mA cm^{-2}, NiFeP@NiP@NF requires an overpotential of 246 mV, which is just 48 mV higher than that of Pt/C@NF. The HER activity of NiFeP@NiP@NF is comparable to high-performance Ni based catalysts as shown in Table S2 only surpassed by trimetallic catalysts. The Tafel slope of NiFeP@NiP@NF is 97.9 mV dec^{-1}, which is smaller than all other synthesized samples. The Tafel slope of Pt/C@NF is much lower (46.2 mV dec^{-1}) indicating a different reaction mechanism on Pt than the Ni-based catalysts. The Tafel slope value suggests that NiFeP@NiP@NF catalyzes hydrogen production via a Volmer-Heyrovsky mechanism with the electrochemical desorption of dihydrogen as the rate determining step.[63] NiFeP@NiP@NF possesses a R_{ct} of 8.2 Ω at -0.20 V, while R_{ct} of NiP@NF and NiFe PBA@NiPO@NF are calculated to be 12.5 and 24.5 Ω, respectively (Figure 4d and Table S5). The small R_{ct} of NiFeP@NiP@NF demonstrates an overall fast electron transfer during HER. Besides activity, stability is a vital criterion for evaluating HER catalysts. Figure 4e represents the HER CP tests of NiFeP@NiP@NF at different current densities, with no obvious decay during the continuous operation over 7 h. Furthermore, a 120 h HER stability test at 10 mA cm^{-2} was conducted on NiFeP@NiP@NF (Figure 4f). At the initial 60 h test, the recorded potential shows negligible changes. However, the overpotential required to reach 10 mA cm^{-2} increases to 207 mV after 120 h (an increase of 86 mV). Polarization curves of NiFeP@NiP@NF tested before and after the 120 h test (inset in Figure 4f) indicates a slight decay of HER activity. For stability test at 500 mA cm^{-2} for 30 h in Figure S17, the potential decreased from -0.501 to -0.521 V after 30 h of continuous testing. Despite insufficient stability, NiFeP@NiP@NF shows the potential to work as the cathode in an alkaline electrolyzer.

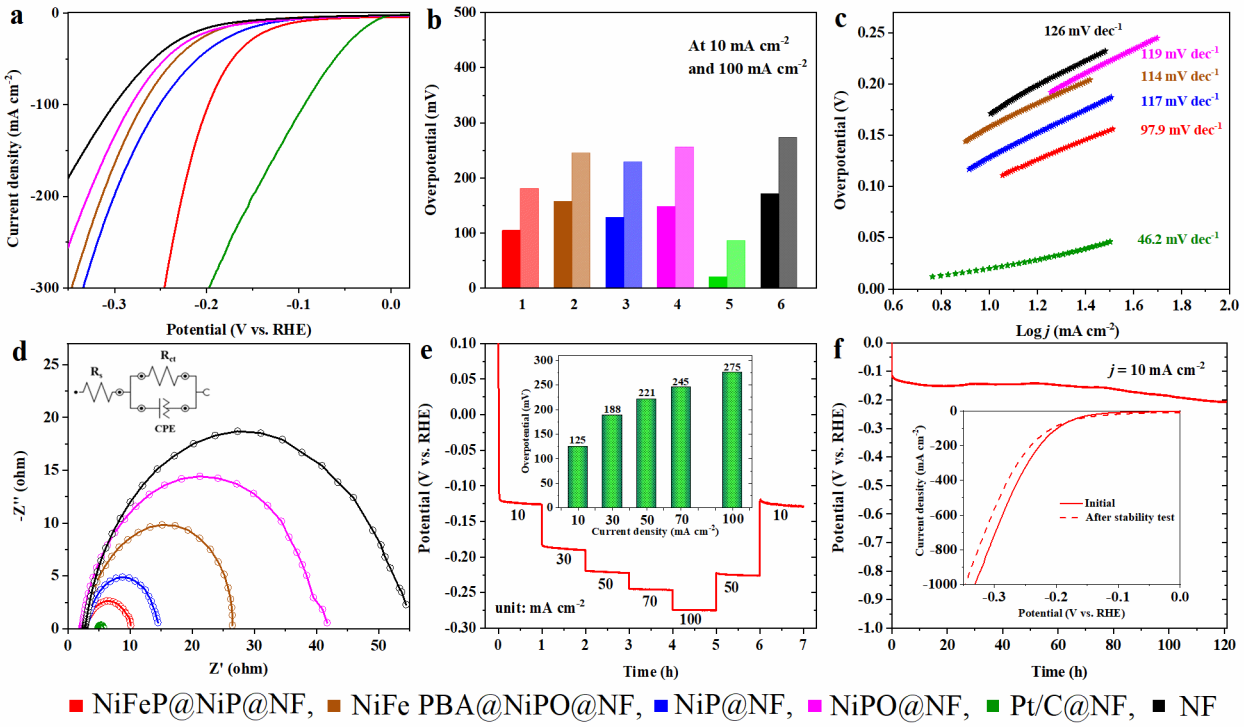

Figure 4. HER performance in 1.0 M KOH. (a) *iR*-corrected polarization curves. Scan rate: 2 mV s^{-1}. (b) Overpotentials at the current densities of 10 mA cm^{-2} and 100 mA cm^{-2}. (c) Tafel plots obtained from the polarization curves in a. (d) Nyquist plots. Inset in (d) is the equivalent circuit used to fit the Nyquist plot. (e) CP tests at different current densities from 10 mA cm^{-2} to 100 mA cm^{-2}. Inset shows overpotentials for delivering different current densities. (f) Long-term stability test of NiFeP@NiP@NF at 10 mA cm^{-2}. Inset: *iR*-corrected polarization curves before and after stability test over 120 h. Scan rate: 2 mV s^{-1}.

The amount of electrocatalytically active sites on NiFeP@NiP@NF and its precursors is roughly probed by the electrochemical surface area (ECSA), proportional to the electrochemical double layer capacitance (C_{dl}, Figure S19). NiFeP@NiP@NF exhibits a much larger ECSA with a C_{dl} value of 4.86 mF cm^{-2}, which is 2.1 times higher than that of NiP@NF. By normalizing to ECSA, the NiFeP@NiP@NF still outperforms NiP@NF for both OER and HER (Figure S20). This

further highlights the advantage of the bimetallic surface of NiFeP@NiP@NF for water splitting and that the performance is not simply boosted by surface area. Through the controllable pyrolysis step, the obtained derivatives of PBAs, such as oxides, sulfides, selenides, and phosphides, could work as excellent candidates for electrocatalytic OER and HER.[46,64–67]

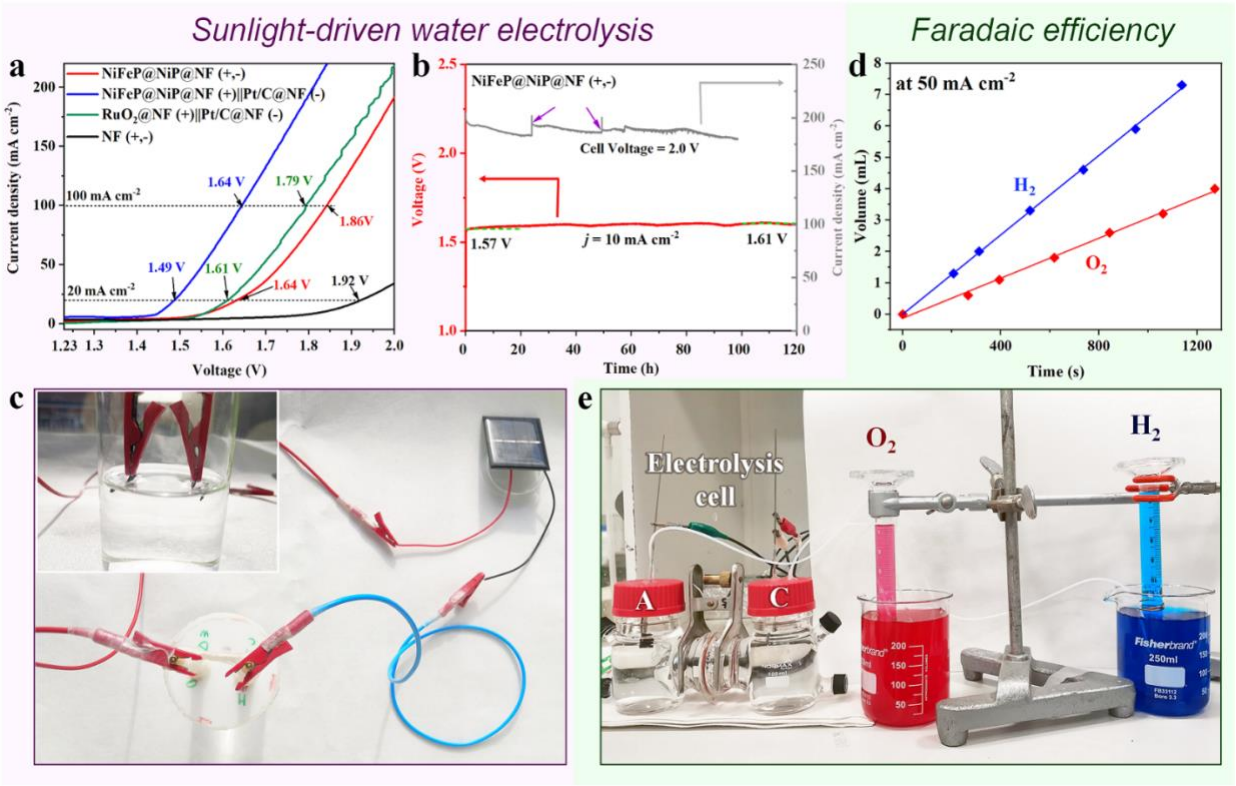

Figure 5. Overall water splitting test with two-electrode systems in 1.0 M KOH. (a) Polarization curves without *iR* compensation for NiFeP@NiP@NF (+,-), NiFeP@NiP@NF (+) and Pt/C (-), RuO_2 (+) and Pt/C (-), and NF (+,-). Scan rate: 2 mV s^{-1}. (b) Long-term stability tests of NiFeP@NiP@NF (+,-) at 10 mA cm^{-2} and 2.0 V, respectively. (c) Photographs of the electrolyzer powered by a commercial solar panel with an open circuit potential of ~2.0 V under sunlight. (d) Plot of displaced volume of water by produced H_2 (blue) and O_2 (red) with time. (e) Photograph of the setup for the measurement of Faradaic efficiency in overall water splitting.

To further demonstrate the promising bifunctional property of NiFeP@NiP@NF, two identical samples are further employed as both the anode and cathode in a two-electrode water splitting setup with 1.0 M KOH electrolyte at RT. A cell voltage of 1.64 V is required to achieve a current density of 20 mA cm^{-2}, very close to that of RuO_2||Pt/C (1.61 V) and much smaller than that of NF||NF (1.92 V), as shown in **Figure 5**a. NiFeP@NiP@NF as the bifunctional catalyst for water splitting is comparable with previously reported non-precious Ni-based bifunctional electrocatalysts (Table S3). Besides, NiFeP@NiP@NF as anode cooperates well with the Pt/C@NF cathode. The cell, NiFeP@NiP@NF (+) and Pt/C@NF (-), yields 20 mA cm^{-2} at the cell voltage of 1.49 V, which is much smaller than the cell voltage required for other electrode couples as shown in Figure 5a. To reach a higher current density of 100 mA cm^{-2}, the symmetric NiFeP@NiP@NF (+, -) requires a cell voltage of 1.86 V, only 0.09 V and 0.24 V higher than RuO_2||Pt/C and NiFeP@NiP@NF||Pt/C@NF, respectively. In addition, the cell NiFeP@NiP@NF(+,-) shows good stability in long-term stability tests. When working at a fixed current density of 10 mA cm^{-2} for 120 h, the required voltage increased by 0.04 V after stability test. When applying a fixed bias of 2.0 V for 98 h (Figure 5b), the current in the circuit decreased slightly from 196 mA cm^{-2} to 180 mA cm^{-2}. During the stability test at 2.0 V, there are large amounts of gas bubbles generated on the surface of both electrodes, which influence the contact between electrodes and electrolyte leading to fluctuations in current density. Removing the bubbles on the electrode by purging the electrolyte with Ar sees the performance of the electrolysis cell recovers as indicated by the purple arrows in Figure 5b. To demonstrate solar to hydrogen generation, a commercial 2 V solar cell (15.75 cm^2) under natural sun light (September in Lyngby, Denmark) was used to drive the symmetric NiFeP@NiP@NF(+,-) cell (Figure 5c), enabling continuous bubble generation. H_2 and O_2 produced by water splitting were collected by the

drainage method as shown in Figure 5d. At the current density of 50 mA cm^{-2}, the volumes of water displacement by H_2 and O_2 production increased linearly with time (Figure 5d). The production rate of H_2 and O_2 was 0.259 μmol s^{-1} and 0.127 μmol s^{-1}, respectively. The Faradaic efficiency for overall water splitting was calculated to be excellent at around 97%. These results highlight that NiFeP@NiP@NF is an excellent bifunctional candidate for overall water splitting.

Microstructure and composition changes of Ni-based phosphides are quite common phenomena during OER and HER processes, which influence the operational stability and practical application of the catalysts.[21,68] Herein, the morphology and composition evolution of NiFeP@NiP@NF working as both the cathode and anode in a two-electrode water splitting setup after the 120 h stability test at 10 mA cm^{-2} are characterized by SEM, XRD, and XPS. Similar XRD patterns of the fresh and spent samples after HER and OER stability tests (Figure S21) suggest that the major crystalline phases have not changed greatly confirming the compositional durability of the core-shell structure. This is further supported by the SEM images (Figure S22) displaying large amounts of rod-like materials still present on the NF framework. However, slight changes after operation are found by comparing the XRD patterns of fresh sample and the samples after OER and HER tests carefully. In Figure S21a, the differences between the XRD patterns of fresh sample and NiFeP@NiP@NF after OER appear around the degree of 34.0, 38.2 and 60.3, which might be broad peaks arising from small $Ni(OH)_2$ (ICSD Coll. Code: 24015) nanoparticles forming during OER operation. After HER testing, a peak at 43.4 degrees appears in the XRD pattern in addition to the three peaks mentioned above, which may be from NiO (ICSD Coll. Code: 92127). XPS is more sensitive than XRD to surface state changes. NiFeP@NiP@NF after OER and HER are therefore also evaluated by XPS analysis (Figure S23 and Figure S24). The low energy peak at 852.6 eV attributed to Ni-P in the Ni 2p spectrum of the fresh NiFeP@NiP@NF (Figure 2c)

disappears after long-term water splitting test on the surface of both electrodes (Figure S23a and S24a). This coincides with the disappearance of the M-P in the P 2p spectrum, in which only a weak broad hump from phosphate species can be observed (Figure S23c and S24c). The XPS-derived atomic ratio of Ni, Fe, and P changes from 1.4:1:6.5 in the fresh NiFeP@NiP@NF to 1.9:1:0.21 and 2.0:1:0.33 in NiFeP@NiP@NF after OER and HER, respectively. The M:P ratio (M = Ni + Fe) increases dramatically from ~0.36 to ~14 and ~9.0 for NiFeP@NiP@NF after OER and HER, respectively. The decrease in the relative P content on the surface could have two reasons: a) dissolution from the metal phosphides into the alkaline electrolyte and b) surface oxidation during electrocatalysis.[46,69]

For the anode where the OER occurs, the general mechanisms in alkaline solution have been proposed as follows:[70,71]

$$M_{cat} + OH^-(aq) \rightarrow M_{cat}OH_{ads} + e^- \quad (1)$$

$$M_{cat}OH_{ads} + OH^-(aq) \rightarrow M_{cat}O_{ads} + H_2O(l) + e^- \quad (2)$$

$$M_{cat}O_{ads} + OH^-(aq) \rightarrow M_{cat}OOH_{ads} + e^- \quad (3)$$

$$M_{cat}OOH_{ads} + OH^-(aq) \rightarrow M_{cat}OO_{ads}^- + H_2O(l) \quad (4)$$

$$M_{cat}OO_{ads}^- \rightarrow M_{cat} + O_2(g) + e^- \quad (5)$$

According to its Tafel slope, steps shown in equation (1) and (2) are both the rate-determining step for NiFeP@NiP@NF.[72,73] During OER process in alkaline electrolyte, NiFeP@NiP@NF works at a potential higher than the oxidation potential of Ni and Fe, and metals atoms (including Ni and Fe) are continuously oxidized to species such as $M_{cat}OH_{ads}$, $M_{cat}O_{ads}$, and $M_{cat}OOH_{ads}$ before O_2 is liberated from the surface. As confirmed by XPS analysis (Figure S23a), a thin layer of metal

hydroxides/oxyhydroxide is formed after OER testing. The outer layer works in synergy with the phosphide core, where the former provides active sites and the latter assists with faster electron diffusion, promoting the OER process.[21]

On the cathode where dihydrogen is generated, the mechanism in alkaline solution is defined as follows according to the Tafel slope:[74]

Volmer step: $M_{cat} + H_2O(l) + e^- \rightarrow M_{cat}H_{ads} + OH^-(aq)$ (6)

Heyrovsky step: $M_{cat}H_{ads} + H_2O(l) + e^- \rightarrow H_2(g) + OH^-(aq) + M_{cat}$ (7)

In the Volmer step, the formation and desorption of OH^- and the adsorption of H atom from adsorbed H_2O could be regarded as the rate-determining steps. OH^- preferentially attaches to oxide sites, while H atoms prefer sites with negative charge. In the composite of NiFeP@NiP@NF, negative P species on the surface of the catalyst could collect protons while the metal oxides from surface oxidation could provide sites for OH^-, facilitating the process of HER.[21,75] Moreover, bimetallic Ni and Fe phosphides derived from NiFe PBA could modify the electronic structure and optimize the hydrogen adsorption energy, leading to a better catalytic activity. Although there is more P in NiFeP@NiP@NF after HER in comparison with NiFeP@NiP@NF after OER, the leaching of P element is thought be the main reason for the degradation of HER performance of NiFeP@NiP@NF in Figure 4f.[21,76]

3. CONCLUSIONS

In summary, NiFeP@NiP@NF with hierarchical structure has been successfully synthesized by the phosphidation of the precursor NiFe PBA@NiPO@NF. In order to reduce the electrical resistance, NiPO rods were directly grown on NF by a microwave-assisted hydrothermal method,

which is more efficient than conventional hydrothermal synthesis. The robust rod-like structure of NiPO@NF synthesized by this method has been rarely reported. NiFe PBA layers were also grown directly on the surface of the NiPO rods by a facile method to ensure intimate contact between the catalyst layer and the conductive support. The NiFe PBA layer helped to maintain the rod-like microstructure in the final phosphidation step to fabricate NiFeP@NiP@NF. For this catalyst, NiFeP derived from NiFe PBA at the surface works as the active material providing abundant active sites for OER and HER, while NiP, mainly derived from NiPO, supports the structure and provides a large active surface area. NiFeP@NiP@NF displays excellent electrocatalytic performance towards both OER and HER in alkaline electrolyte, requiring low overpotentials of 227 and 105 mV, respectively, to achieve a current density of 10 mA cm^{-2}. A symmetrical electrolyzer using two NiFeP@NiP@NF electrodes only requires a cell voltage of 1.64 V to deliver 20 mA cm^{-2}, and exhibits robust stability over 120 h at 10 mA cm^{-2}. Furthermore, the electrolyzer cell was operated at relatively high current density (~180 mA cm^{-2}) by applying a fixed bias of 2.0 V providing good stability over 100 h. The excellent catalytic activity and stability of NiFeP@NiP@NF are attributed to the following aspects: (1) NiFeP layer derived from NiFe PBA provides a large surface area and a composite nickel and iron phosphide, providing more active sites and a modified electronic structure with enhanced activity. (2) The hierarchical structure enables the utilization of the good conductivity of the nickel phosphide rods and NF to reduce resistance losses and thus facilitate high reaction rates. (3) The rod structure on NF can be maintained preventing structural degradation and delamination caused by H_2 and O_2 bubbles generated during water splitting in the course of long-term application. The synthesis method and design can further be extended to the fabrication of other inexpensive multicomponent catalyst materials.

4. EXPERIMENTAL SECTION

Chemicals and Materials: Nickel(II) nitrate hexahydrate ($Ni(NO_3)_2 \cdot 6H_2O$, 97.0%), hydrochloric acid (HCl, 37 wt%, 1.2 g mL^{-1} at 25 °C), platinum on graphitized carbon black (Pt/C, 20 wt% Pt loading on Vulcan XC72), iron(III) chloride hexahydrate ($FeCl_3 \cdot 6H_2O$, ≥97%), sodium hypophosphite monohydrate ($NaH_2PO_2 \cdot H_2O$, ≥99%), ruthenium(IV) oxide (RuO_2, ≥99.9%), Nafion® perfluorinated ion-exchange resin (10 wt% dispersion in water), ammonium dihydrogen phosphate ($NH_4H_2PO_4$, ≥99%) and trisodium citrate dihydrate ($C_6H_5Na_3O_7 \cdot 2H_2O$, ≥99%) were obtained from Sigma-Aldrich. Nickel(II) chloride hexahydrate ($NiCl_2 \cdot 6H_2O$, ≥98%) was purchased from BDH Chemicals. Potassium hexacyanoferrate(III) ($K_3Fe(CN)_6$, ≥99%) was purchased from Riedel-de Haën. 1.0 M potassium hydroxide (KOH, pH 14) solution was purchased from Fisher Chemical. All chemicals were used directly as received. All aqueous solutions were prepared with 18.2 MΩ·cm ultrapure water (arium® pro VF Ultrapure Water System, Sartorius AG, Germany). NF sheets with a thickness of 300 μm were purchased from Suzhou Jiashide Metal Foam Co., Ltd., China. Prior to use, NF was cleaned with ethanol, 1.0 M HCl solution, and water successively under ultrasonication to remove contaminants and nickel oxides from the surface.

Synthesis of NiPO@NF: Nickel phosphate hydrate (NiPO, $Ni_3(PO_4)_2 \cdot 8H_2O$) rods were grown on NF (NiPO@NF) by a microwave-assisted method. In a typical synthesis, 0.10 mmol $NiCl_2 \cdot 6H_2O$, 0.05 mmol $FeCl_3 \cdot 6H_2O$, and 0.21 mmol $NH_4H_2PO_4$ were dispersed in 15 mL water under vigorous stirring for 30 min at RT. The obtained solution was then transferred into a 10-20 mL microwave reaction vial containing a piece of NF (1×3 cm^2). The sealed vials were heated in a microwave synthesizer (Biotage Initiator, Biotage, Sweden) at 180 ℃ for 60 min. After the vial had cooled to RT, the sample was washed with water five times before it was dried in a vacuum oven at 80 ℃ for 8 h. As reference, two samples were prepared without adding either $FeCl_3 \cdot 6H_2O$ or both $NiCl_2 \cdot 6H_2O$ and $FeCl_3 \cdot 6H_2O$ to the growth solution.

Synthesis of NiFe PBA@NiPO@NF: NiFe PBA (potassium nickel hexacyanoferrate(III), $KNiFe(CN)_6$) were grown on the surface of the NiPO rods by a facile precipitation method.[66] 10 mL aqueous solution of 20 mM $K_3[Fe(CN)_6]$ was slowly poured into a stirred 10 mL mixture containing 45 mM trisodium citrate and 30 mM $Ni(NO_3)_2$ and stirring maintained for 10 min. Then, a piece of NiPO@NF was immersed in the mixture, which was transferred to an oven and kept at 40 ℃ for different durations (1, 3, 6, 12 and 24 h). Finally, the obtained samples were rinsed with water five times following a drying treatment at 80 ℃ for 8 h in a vacuum oven. The samples with different reaction durations are denoted as NiFe PBA@NiPO@NF-*t*, where t represents the NiFe PBA growth time. If not specified, NiFe PBA@NiPO@NF refers to the sample NiFe PBA@NiPO@NF-6 h. NiFe PBA directly grown on NF for 6 h (NiFe PBA@NF) was prepared following the same procedure by replacing NiPO@NF with NF.

Synthesis of NiFeP@NiP@NF: In a typical synthesis, a dry piece of as-prepared NiFe PBA@NiPO@NF and 0.50 g $NaH_2PO_2 \cdot H_2O$ were put in two porcelain boats in a tube furnace with $NaH_2PO_2 \cdot H_2O$ at the upstream. The tube furnace was heated to different temperatures (250, 350,

450 and 550 ℃) with a heating rate of 2 ℃ min^{-1} under Ar atmosphere and kept at the chosen temperature for 2 h. The samples obtained this phosphidation step are distinguished as NiFeP@NiP@NF-*T*, where *T* represents the calcination temperature. If not specified, NiFeP@NiP@NF refers to the NiFeP@NiP@NF-450 ℃ sample. NiFeP@NF was also prepared as a control by phosphidation of NiFe PBA@NF at 450 ℃. Caution: Ensuring a leak-free environment in the tube furnace and safe management of the furnace exhaust during the reaction are crucial to avoid exposure to toxic gaseous byproducts (PH_3).

Materials characterizations: Powder XRD patterns were acquired with a Huber G670 Guinier camera using Cu-Kα radiation (λ=1.5406 Å). XPS data were collected on a Thermo Scientific K-Alpha XPS spectrometer. The material morphology was characterized using a SEM (FEI Quanta FEG 250 Analytical ESEM) with EDS. FT-IR spectra were obtained on a Bruker Alpha-P FT-IR spectrophotometer. Raman spectra in a Stokes-shift range of 50−4000 cm^{-1} were recorded on a Horiba XploRa Plus confocal Raman microscope (excitation wavelength: 532 nm, excitation power: 4 mW, acquisition time: 30 s, accumulations: 10, grating: 1200 g mm^{-1}, confocal aperture: 300 µm, slit: 100 µm). Transmission electron microscopy (TEM), high-resolution TEM (HRTEM), and the corresponding EDS characterization were performed on a Tecnai T20 G2 at 200 kV equipped with a TVIPS XF416 4k × 4k camera. Electrochemical characterization: The electrochemical performance was measured with either an Autolab PGSTAT12 (Metrohm Autolab, the Netherlands), a CHI 760C electrochemical workstation (CH Instruments, Inc. USA) or a PalmSens3 compact electrochemical interface (PalmSens BV, the Netherlands). A typical three-electrode system was used with the active material on NF as the working electrode, a carbon rod counter electrode, an Ag/AgCl (saturated KCl) reference electrode, and 1.0 M KOH electrolyte. All potentials were converted to the reversible hydrogen electrode (RHE) scale through the

following equation: E (vs. RHE) = E (vs. Ag/AgCl) + 0.197 + 0.059 × pH. OER and HER overpotentials (η) were calculated based on the following equations: $\eta_{OER} = E$ (vs. RHE) - 1.23 V; for HER, η_{HER} = 0 V - E (vs. RHE). Linear sweep voltammetry (LSV) and cyclic voltammetry (CV) were conducted at a scan rate of 2 mV s^{-1}. The overpotential at 10 mA cm^{-2} for OER of the NiFeP@NiP@NF without *iR* correction was taken after 0.5 h of the CP testing at 10 mA cm^{-2}. Otherwise, overpotentials reported in this work were taken from *iR*-corrected LSV curves. The solution was quiescent during electrochemical tests. LSV and CV curves for OER and HER were collected without *iR* correction unless otherwise specified. Electrochemical impedance spectroscopy (EIS) measurements were carried out at 1.50 V for OER and -0.20 V for HER in a frequency range of 10^4–10^{-2} Hz and an amplitude voltage of 5 mV. For comparison, benchmark Pt/C and RuO_2 were painted on NF with a mass loading of 3.0 mg cm^{-2}. ECSA of a catalyst was assessed by the C_{dl}. CV curves in the potential range of 0.65 V−0.75 V (vs. RHE) at different scan rates of 10, 30, 50, 70, and 90 mV s^{-1} were recorded. C_{dl} was calculated by plotting the half of the current variation ($\Delta J = J_a - J_c$) at 0.72 V (vs. RHE) against the scan rate. The linear slope of the curve is equal to the value of C_{dl}. The overall water splitting test was performed in a two-electrode electrolysis cell in 1.0 M KOH at RT. Long-term stability was evaluated by CP and amperometric *i-t* methods. Reported potentials or voltages tested by CP and *i-t* methods are all read after 0.5 h of test to ensure a stable reading. For the Faradaic efficiency test in overall water splitting, the drainage method was used. A constant current of 50 mA was applied to the two-electrode electrolyzer with electrode areas of 1.0 cm^{-2} for about 1300 s. During the experiment, the volumes of water displaced by evolved H_2 and O_2 were monitored. Faradaic efficiency could be calculated by comparing the experimental gas production and theoretical gas production assuming ideal gas conditions.[77]

ASSOCIATED CONTENT

Supporting Information.

Supporting Information is available free of charge.

Supplementary SEM images, XRD patterns, FT-IR spectra, XPS spectra and Raman spectra of control samples. Supplementary electrochemical polarization curves. Electrochemical-double-layer capacitance measurement in non-faradaic region. Post-test characterization. Supplementary summarizing tables. (file type: PDF)

AUTHOR INFORMATION

Corresponding Author(s)

Christian Engelbrekt – Department of Chemistry, Technical University of Denmark, DK-2800 Kongens Lyngby, Denmark. E-mail: cheng@kemi.dtu.dk

Xinxin Xiao – Department of Chemistry, Technical University of Denmark, DK-2800 Kongens Lyngby, Denmark. E-mail: xixiao@kemi.dtu.dk

Authors

Fangyuan Diao – Department of Chemistry, Technical University of Denmark, DK-2800 Kongens Lyngby, Denmark

Wei Huang – Department of Chemistry, Technical University of Denmark, DK-2800 Kongens Lyngby, Denmark.

Georgios Ctistis – Institut für Nanophotonik Göttingen e.V., Department of Photonic Sensor Technology, Hans-Adolf-Krebs-Weg 1, 37077 Göttingen, Germany

Hainer Wackerbarth – Institut für Nanophotonik Göttingen e.V., Department of Photonic Sensor Technology, Hans-Adolf-Krebs-Weg 1, 37077 Göttingen, Germany

Yuan Yang – Key Laboratory for Liquid-Solid Structural Evolution and Processing of Materials (Ministry of Education), Research Center for Carbon Nanomaterials, School of Materials Science and Engineering, Shandong University, Jinan 250061, P. R.

Pengchao Si – Key Laboratory for Liquid-Solid Structural Evolution and Processing of Materials (Ministry of Education), Research Center for Carbon Nanomaterials, School of Materials Science and Engineering, Shandong University, Jinan 250061, P. R.

Jingdong Zhang – Department of Chemistry, Technical University of Denmark, DK-2800 Kongens Lyngby, Denmark

Author Contributions

The manuscript was written through contributions of all authors. C.E. and X.X. supervised and reviewed this work. F.D. designed the experiments, analyzed data and prepared the manuscript. W.H., Y.Y., and P.S. offered help in electrochemical and structural analyses. G.C. and H.W. performed Raman tests and structural analyses. All authors have given approval to the final version of the manuscript.

Funding Sources

China Scholarship Council (201806220068). Villum Experiment (grant No. 35844).

Notes

All authors have no conflicts of interest.

ACKNOWLEDGMENT

Fangyuan Diao thanks the support of China Scholarship Council (201806220068). Xinxin Xiao acknowledges the Villum Experiment (grant No. 35844).

ABBREVIATIONS

OER, oxygen evolution reaction; NiFeP@NiP@NF, NiFeP catalyst coated on nickel phosphide rods on nickel foam; H_2, hydrogen; HER, hydrogen evolution reaction; TMPs, transition metal phosphides; NF, nickel foam; NiFe PBA, NiFe Prussian blue analogue; NiPO, nickel phosphate hydrate; NiFe PBA@NiPO@NF, NiFe Prussian blue analogue formed on nickel phosphate hydrate rods grown on NF; NiPO@NF, nickel phosphate hydrate rods constructed on the surface of nickel foam; XRD, X-ray diffraction; ICSD Coll. Code, Inorganic Crystal Structure Database Collection Code; EDS, energy dispersive spectroscopy; FT-IR, Fourier transform infrared; SEM, scanning electron microscope; XPS, X-ray photoelectron spectroscopy; RT, room temperature; NiP@NF, prepared by phosphidation of NiPO@NF; RuO_2@NF, RuO_2 paste on NF; NiFe PBA@NF, NiFe PBA grown directly on nickel foam; NiFeP@NF, prepared by phosphidation of NiFe PBA@NF; R_{ct}, charge transfer resistance; CP, chronopotentiometry; Pt/C@NF, commercial 20 wt.% platinum on graphitized carbon black pasted on nickel foam; ECSA, electrochemical surface area; C_{dl}, electrochemical double layer capacitance; TEM, transmission electron microscopy; HRTEM, high-resolution TEM; RHE, reversible hydrogen electrode; LSV, linear sweep voltammetry; CV, cyclic voltammetry; EIS, electrochemical impedance spectroscopy.

REFERENCES

(1) Alanne, K.; Cao, S. Zero-Energy Hydrogen Economy (ZEH_2E) for Buildings and Communities Including Personal Mobility. *Renew. Sustain. Energy Rev.* **2017**, *71*, 697–711.

(2) Brandon, N. P.; Kurban, Z. Clean Energy and the Hydrogen Economy. *Philos. Trans. R. Soc. A Math. Phys. Eng. Sci.* **2017**, *375*, 20160400.

(3) Abe, J. O.; Popoola, A. P. I.; Ajenifuja, E.; Popoola, O. M. Hydrogen Energy, Economy and Storage: Review and Recommendation. *Int. J. Hydrogen Energy* **2019**, *44*, 15072–15086.

(4) Chen, S.; Kharrazi, A.; Liang, S.; Fath, B. D.; Lenzen, M.; Yan, J. Advanced Approaches and Applications of Energy Footprints toward the Promotion of Global Sustainability. *Appl. Energy* **2020**, *261*,114415.

(5) Demirbas, A. Future Hydrogen Economy and Policy. *Energy Sources, Part B Econ. Plan. Policy* **2017**, *12* (2), 172–181.

(6) Peng, Z.; Liu, J.; Hu, B.; Yang, Y.; Guo, Y.; Li, B.; Li, L.; Zhang, Z.; Cui, B.; He, L.; Du, M. Surface Engineering on Nickel-Ruthenium Nanoalloys Attached Defective Carbon Sites as Superior Bifunctional Electrocatalysts for Overall Water Splitting. *ACS Appl. Mater. Interfaces* **2020**, *12* (12), 13842–13851.

(7) Jeong, J. H.; Kunwar, S.; Pandit, S.; Lee, J. CoP_2 Nanoparticles Deposited on Nanometer-Thick Pt-Coated Fluorine-Doped Tin Oxide Substrates as Electrocatalysts for Simultaneous Hydrogen Evolution and Oxygen Evolution. *ACS Appl. Nano Mater.* **2020**, *3* (7), 6507–6515.

(8) Li, Z.; Ge, R.; Su, J.; Chen, L. Recent Progress in Low Pt Content Electrocatalysts for Hydrogen Evolution Reaction. *Adv. Mater. Interfaces* **2020**, *7* (14), 2000396.

(9) Shen, F.; Wang, Y.; Qian, G.; Chen, W.; Jiang, W.; Luo, L.; Yin, S. Bimetallic Iron-Iridium Alloy Nanoparticles Supported on Nickel Foam as Highly Efficient and Stable Catalyst for Overall Water Splitting at Large Current Density. *Appl. Catal. B Environ.* **2020**, *278*, 119327.

(10) Yu, T.; Xu, Q.; Qian, G.; Chen, J.; Zhang, H.; Luo, L.; Yin, S. Amorphous CoO_x-Decorated Crystalline RuO_2 Nanosheets as Bifunctional Catalysts for Boosting Overall Water Splitting at

Large Current Density. *ACS Sustain. Chem. Eng.* **2020**, *8* (47), 17520–17526.

(11) Cherevko, S.; Geiger, S.; Kasian, O.; Kulyk, N.; Grote, J. P.; Savan, A.; Shrestha, B. R.; Merzlikin, S.; Breitbach, B.; Ludwig, A.; Mayrhofer, K. J. J. Oxygen and Hydrogen Evolution Reactions on Ru, RuO_2, Ir, and IrO_2 Thin Film Electrodes in Acidic and Alkaline Electrolytes: A Comparative Study on Activity and Stability. *Catal. Today* **2016**, *262*, 170–180.

(12) Ye, S.; Luo, F.; Zhang, Q.; Zhang, P.; Xu, T.; Wang, Q.; He, D.; Guo, L.; Zhang, Y.; He, C.; Ouyang, X.; Gu, M.; Liu, J.; Sun, X. Highly Stable Single Pt Atomic Sites Anchored on Aniline-Stacked Graphene for Hydrogen Evolution Reaction. *Energy Environ. Sci.* **2019**, *12* (3), 1000–1007.

(13) Kemppainen, E.; Bodin, A.; Sebok, B.; Pedersen, T.; Seger, B.; Mei, B.; Bae, D.; Vesborg, P. C. K.; Halme, J.; Hansen, O.; Lund, P. D.; Chorkendorff, I. Scalability and Feasibility of Photoelectrochemical H_2 Evolution: The Ultimate Limit of Pt Nanoparticle as an HER Catalyst. *Energy Environ. Sci.* **2015**, *8* (10), 2991–2999.

(14) Zou, X.; Zhang, Y. Noble Metal-Free Hydrogen Evolution Catalysts for Water Splitting. *Chem. Soc. Rev.* **2015**, *44* (15), 5148–5180.

(15) Wu, Z. P.; Lu, X. F.; Zang, S. Q.; Lou, X. W. Non-Noble-Metal-Based Electrocatalysts toward the Oxygen Evolution Reaction. *Adv. Funct. Mater.* **2020**, *30* (15), 1910274.

(16) Huang, W.; Tang, J.; Diao, F.; Engelbrekt, C.; Ulstrup, J.; Xiao, X.; Mølhave, K. Recent Progress of 2D Metal-organic Frameworks and Their Derivatives for Oxygen Evolution Electrocatalysis. *ChemElectroChem* **2020**. DOI 10.1002/celc.202001137.

(17) Anantharaj, S.; Ede, S. R.; Sakthikumar, K.; Karthick, K.; Mishra, S.; Kundu, S. Recent Trends and Perspectives in Electrochemical Water Splitting with an Emphasis on Sulfide, Selenide, and Phosphide Catalysts of Fe, Co, and Ni: A Review. *ACS Catal.* **2016**, *6* (12), 8069–

8097.

(18) Tian, J.; Liu, Q.; Asiri, A. M.; Sun, X. Self-Supported Nanoporous Cobalt Phosphide Nanowire Arrays: An Efficient 3D Hydrogen-Evolving Cathode over the Wide Range of PH 0-14. *J. Am. Chem. Soc.* **2014**, *136* (21), 7587–7590.

(19) Liu, P.; Rodriguez, J. A. Catalysts for Hydrogen Evolution from the [NiFe] Hydrogenase to the Ni 2P(001) Surface: The Importance of Ensemble Effect. *J. Am. Chem. Soc.* **2005**, *127* (42), 14871–14878.

(20) Liu, K.; Wang, F.; He, P.; Shifa, T. A.; Wang, Z.; Cheng, Z.; Zhan, X.; He, J. The Role of Active Oxide Species for Electrochemical Water Oxidation on the Surface of 3d-Metal Phosphides. *Adv. Energy Mater.* **2018**, *8* (15), 1703290.

(21) Menezes, P. W.; Indra, A.; Das, C.; Walter, C.; Göbel, C.; Gutkin, V.; Schmeißer, D.; Driess, M. Uncovering the Nature of Active Species of Nickel Phosphide Catalysts in High-Performance Electrochemical Overall Water Splitting. *ACS Catal.* **2017**, *7* (1), 103–109.

(22) Pu, Z.; Saana Amiinu, I.; Wang, M.; Yang, Y.; Mu, S. Semimetallic MoP_2: An Active and Stable Hydrogen Evolution Electrocatalyst over the Whole PH Range. *Nanoscale* **2016**, *8* (16), 8500–8504.

(23) Wu, Z.; Wang, J.; Liu, R.; Xia, K.; Xuan, C.; Guo, J.; Lei, W.; Wang, D. Facile Preparation of Carbon Sphere Supported Molybdenum Compounds (P, C and S) as Hydrogen Evolution Electrocatalysts in Acid and Alkaline Electrolytes. *Nano Energy* **2017**, *32*, 511–519.

(24) Pu, Z.; Wei, S.; Chen, Z.; Mu, S. Flexible Molybdenum Phosphide Nanosheet Array Electrodes for Hydrogen Evolution Reaction in a Wide PH Range. *Appl. Catal. B Environ.* **2016**, *196*, 193–198.

(25) Popczun, E. J.; Read, C. G.; Roske, C. W.; Lewis, N. S.; Schaak, R. E. Highly Active

Electrocatalysis of the Hydrogen Evolution Reaction by Cobalt Phosphide Nanoparticles. *Angew. Chemie* **2014**, *126* (21), 5531–5534.

(26) Jiang, P.; Liu, Q.; Liang, Y.; Tian, J.; Asiri, A. M.; Sun, X. A Cost-Effective 3D Hydrogen Evolution Cathode with High Catalytic Activity: FeP Nanowire Array as the Active Phase. *Angew. Chemie* **2014**, *126* (47), 13069–13073.

(27) Yu, F.; Zhou, H.; Huang, Y.; Sun, J.; Qin, F.; Bao, J.; Goddard, W. A.; Chen, S.; Ren, Z. High-Performance Bifunctional Porous Non-Noble Metal Phosphide Catalyst for Overall Water Splitting. *Nat. Commun.* **2018**, *9* (1), 1–9.

(28) Popczun, E. J.; McKone, J. R.; Read, C. G.; Biacchi, A. J.; Wiltrout, A. M.; Lewis, N. S.; Schaak, R. E. Nanostructured Nickel Phosphide as an Electrocatalyst for the Hydrogen Evolution Reaction. *J. Am. Chem. Soc.* **2013**, *135* (25), 9267–9270.

(29) Yang, S.; Chen, G.; Ricciardulli, A. G.; Zhang, P.; Zhang, Z.; Shi, H.; Ma, J.; Zhang, J.; Blom, P. W. M.; Feng, X. Topochemical Synthesis of Two-Dimensional Transition-Metal Phosphides Using Phosphorene Templates. *Angew. Chemie - Int. Ed.* **2020**, *59* (1), 465–470.

(30) Mendoza-Garcia, A.; Su, D.; Sun, S. Sea Urchin-like Cobalt-Iron Phosphide as an Active Catalyst for Oxygen Evolution Reaction. Nanoscale 2016, 8 (6), 3244–3247.

(31) Wu, R.; Xiao, B.; Gao, Q.; Zheng, Y.; Zheng, X.; Zhu, J.; Gao, M.; Yu, S. A Janus Nickel Cobalt Phosphide Catalyst for High-Efficiency Neutral-pH Water Splitting. Angew. Chemie 2018, 130 (47), 15671–15675.

(32) Xu, X.; Tian, X.; Zhong, Z.; Kang, L.; Yao, J. In-Situ Growth of Iron/Nickel Phosphides Hybrid on Nickel Foam as Bifunctional Electrocatalyst for Overall Water Splitting. J. Power Sources 2019, 424, 42–51.

(33) Qiu, B.; Cai, L.; Wang, Y.; Lin, Z.; Zuo, Y.; Wang, M.; Chai, Y. Fabrication of Nickel–

Cobalt Bimetal Phosphide Nanocages for Enhanced Oxygen Evolution Catalysis. Adv. Funct. Mater. 2018, 28 (17), 1–9.

(34) Kibsgaard, J.; Tsai, C.; Chan, K.; Benck, J. D.; Nørskov, J. K.; Abild-Pedersen, F.; Jaramillo, T. F. Designing an Improved Transition Metal Phosphide Catalyst for Hydrogen Evolution Using Experimental and Theoretical Trends. Energy Environ. Sci. 2015, 8 (10), 3022–3029.

(35) Ren, J. T.; Wang, Y. S.; Chen, L.; Gao, L. J.; Tian, W. W.; Yuan, Z. Y. Binary FeNi Phosphides Dispersed on N,P-Doped Carbon Nanosheets for Highly Efficient Overall Water Splitting and Rechargeable Zn-Air Batteries. *Chem. Eng. J.* **2020**, *389*, 124408.

(36) Colli, A. N.; Girault, H. H.; Battistel, A. Non-Precious Electrodes for Practical Alkaline Water Electrolysis. *Materials* **2019**, *12* (8), 1–17.

(37) Rakousky, C.; Keeley, G. P.; Wippermann, K.; Carmo, M.; Stolten, D. The Stability Challenge on the Pathway to High-Current-Density Polymer Electrolyte Membrane Water Electrolyzers. *Electrochim. Acta* **2018**, *278*, 324–331.

(38) Ahn, S. H.; Manthiram, A. Direct Growth of Ternary Ni-Fe-P Porous Nanorods onto Nickel Foam as a Highly Active, Robust Bi-Functional Electrocatalyst for Overall Water Splitting. *J. Mater. Chem. A* **2017**, *5* (6), 2496–2503.

(39) Ray, C.; Lee, S. C.; Jin, B.; Kundu, A.; Park, J. H.; Jun, S. C. Stacked Porous Iron-Doped Nickel Cobalt Phosphide Nanoparticle: An Efficient and Stable Water Splitting Electrocatalyst. *ACS Sustain. Chem. Eng.* **2018**, *6* (5), 6146–6156.

(40) Cao, Q.; Wang, C.; Chen, S.; Xu, X.; Liu, F.; Geng, X.; Wang, J. Vertically Aligned NiP_2 Nanosheets with Interlaced Mesh Network for Highly Efficient Water Splitting under Alkaline and Acid Solutions. *Int. J. Hydrogen Energy* **2019**, *44* (13), 6535–6543.

(41) Xiao, X.; Engelbrekt, C.; Zhang, M.; Li, Z.; Ulstrup, J.; Zhang, J.; Si, P. A Straight Forward Approach to Electrodeposit Tungsten Disulfide/Poly(3,4-Ethylenedioxythiophene) Composites onto Nanoporous Gold for the Hydrogen Evolution Reaction. *Appl. Surf. Sci.* **2017**, *410*, 308–314.

(42) Guan, Q.; Li, W.; Zhang, M.; Tao, K. Alternative Synthesis of Bulk and Supported Nickel Phosphide from the Thermal Decomposition of Hypophosphites. *J. Catal.* **2009**, *263* (1), 1–3.

(43) Noisong, P.; Danvirutai, C.; Srithanratana, T.; Boonchom, B. Synthesis, Characterization and Non-Isothermal Decomposition Kinetics of Manganese Hypophosphite Monohydrate. *Solid State Sci.* **2008**, *10* (11), 1598–1604.

(44) Al-Omair, M. A.; Touny, A. H.; Saleh, M. M. Reflux-Based Synthesis and Electrocatalytic Characteristics of Nickel Phosphate Nanoparticles. *J. Power Sources* **2017**, *342*, 1032–1039.

(45) Kullyakool, S.; Danvirutai, C.; Siriwong, K.; Noisong, P. Determination of Kinetic Triplet of the Synthesized $Ni_3(PO_4)_2 \cdot 8H_2O$ by Non-Isothermal and Isothermal Kinetic Methods. *J. Therm. Anal. Calorim.* **2014**, *115* (2), 1497–1507.

(46) Xiang, R.; Duan, Y.; Tong, C.; Peng, L.; Wang, J.; Shah, S. S. A.; Najam, T.; Huang, X.; Wei, Z. Self-Standing FeCo Prussian Blue Analogue Derived FeCo/C and FeCoP/C Nanosheet Arrays for Cost-Effective Electrocatalytic Water Splitting. *Electrochim. Acta* **2019**, *302*, 45–55.

(47) Han, L.; Tang, P.; Reyes-Carmona, Á.; Rodríguez-García, B.; Torréns, M.; Morante, J. R.; Arbiol, J.; Galan-Mascaros, J. R. Enhanced Activity and Acid pH Stability of Prussian Blue-Type Oxygen Evolution Electrocatalysts Processed by Chemical Etching. *J. Am. Chem. Soc.* **2016**, *138* (49), 16037–16045.

(48) Ge, Y.; Dong, P.; Craig, S. R.; Ajayan, P. M.; Ye, M.; Shen, J. Transforming Nickel

Hydroxide into 3D Prussian Blue Analogue Array to Obtain Ni_2P/Fe_2P for Efficient Hydrogen Evolution Reaction. *Adv. Energy Mater.* **2018**, *8* (21), 1–9.

(49) Zou, H. H.; Yuan, C. Z.; Zou, H. Y.; Cheang, T. Y.; Zhao, S. J.; Qazi, U. Y.; Zhong, S. L.; Wang, L.; Xu, A. W. Bimetallic Phosphide Hollow Nanocubes Derived from a Prussian-Blue-Analog Used as High-Performance Catalysts for the Oxygen Evolution Reaction. *Catal. Sci. Technol.* **2017**, *7* (7), 1549–1555.

(50) Ng, C. W.; Ding, J.; Gan, L. M. Microstructural Changes Induced by Thermal Treatment of Cobalt(II) Hexacyanoferrate(III) Compound. *J. Solid State Chem.* **2001**, *156* (2), 400–407.

(51) Xiong, P.; Zeng, G.; Zeng, L.; Wei, M. Prussian Blue Analogues $Mn[Fe(CN)_6]_{0.6667}\cdot nH_2O$ Cubes as an Anode Material for Lithium-Ion Batteries. *Dalt. Trans.* **2015**, *44* (38), 16746–16751.

(52) Zhang, W.; Zhao, Y.; Malgras, V.; Ji, Q.; Jiang, D.; Qi, R.; Ariga, K.; Yamauchi, Y.; Liu, J.; Jiang, J. Sen; Hu, M. Synthesis of Monocrystalline Nanoframes of Prussian Blue Analogues by Controlled Preferential Etching. *Angew. Chemie - Int. Ed.* **2016**, *55* (29), 8228–8234.

(53) Zhang, W.; Zhao, Y.; Malgras, V.; Ji, Q.; Jiang, D.; Qi, R.; Ariga, K.; Yamauchi, Y.; Liu, J.; Jiang, J. Sen; Hu, M. Synthesis of Monocrystalline Nanoframes of Prussian Blue Analogues by Controlled Preferential Etching. *Angew. Chemie - Int. Ed.* **2016**, *55* (29), 8228–8234.

(54) Cuesta, A.; Dhamelincourt, P.; Laureyns, J.; Martínez-Alonso, A.; Tascón, J. M. D. Raman Microprobe Studies on Carbon Materials. *Carbon N. Y.* **1994**, *32* (8), 1523–1532.

(55) Eliche-Quesada, D.; Mérida-Robles, J.; Maireles-Torres, P.; Rodríguez-Castellón, E.; Jiménez-López, A. Hydrogenation and Ring Opening of Tetralin on Supported Nickel Zirconium-Doped Mesoporous Silica Catalysts. Influence of the Nickel Precursor. *Langmuir* **2003**, *19* (12), 4985–4991.

(56) Grosvenor, A. P.; Biesinger, M. C.; Smart, R. S. C.; McIntyre, N. S. New Interpretations of XPS Spectra of Nickel Metal and Oxides. *Surf. Sci.* **2006**, *600* (9), 1771–1779.

(57) Guan, Q.; Cheng, X.; Li, R.; Li, W. A Feasible Approach to the Synthesis of Nickel Phosphide for Hydrodesulfurization. *J. Catal.* **2013**, *299* (3), 1–9.

(58) Lee, B.; Kim, C.; Park, Y.; Kim, T. G.; Park, B. Nanostructured Platinum/Iron Phosphate Thin-Film Electrodes for Methanol Oxidation. *Electrochem. Solid-State Lett.* **2006**, *9* (10), E27.

(59) Grosseau-Poussard, J. L.; Panicaud, B.; Pedraza, F.; Renault, P. O.; Silvain, J. F. Iron Oxidation under the Influence of Phosphate Thin Films. *J. Appl. Phys.* **2003**, *94* (1), 784–788.

(60) Qian, X.; Qin, H.; Meng, T.; Lin, Y.; Ma, Z. Metal Phosphate-Supported Pt Catalysts for CO Oxidation. *Materials* **2014**, *7* (12), 8105–8130.

(61) Baghendra, S.; Arindam, I. Prussian blue- and Prussian blue analogue-derived materials: progress and prospects for electrochemical energy conversion. *Materials Today Energy* **2020**, *16*, 100404

(62) Dong, C.; Wang, X.; Liu, X.; Yuan, X.; Dong, W.; Cui, H.; Duan, Y.; Huang, F. In Situ Grown Nb_4N_5 Nanocrystal on Nitrogen-Doped Graphene as a Novel Anode for Lithium Ion Battery. *RSC Adv.* **2016**, *6* (84), 81290–81295.

(63) Niu, Z.; Qiu, C.; Jiang, J.; Ai, L. Hierarchical CoP-FeP Branched Heterostructures for Highly Efficient Electrocatalytic Water Splitting. *ACS Sustain. Chem. Eng.* **2019**, *7* (2), 2335–2342.

(64) Xu, H.; Ye, K.; Zhu, K.; Gao, Y.; Yin, J.; Yan, J.; Wang, G.; Cao, D. Transforming Carnation-Shaped MoF-Ni to Ni−Fe Prussian Blue Analogue Derived Efficient Bifunctional Electrocatalyst for Urea Electrolysis. *ACS Sustain. Chem. Eng.* **2020**, *8* (42), 16037–16045.

(65) Ma, F.; Wu, Q.; Liu, M.; Zheng, L.; Tong, F.; Wang, Z.; Wang, P.; Liu, Y.; Cheng, H.; Dai,

Y.; Zheng, Z.; Fan, Y.; Huang, B. Surface Fluorination Engineering of NiFe Prussian Blue Analogue Derivatives for Highly Efficient Oxygen Evolution Reaction. *ACS Appl. Mater. Interfaces* **2021**, *13* (4), 5142–5152.

(66) Yu, X.-Y.; Yu, L.; Wu, H. Bin; Lou, X. W. D. Formation of Nickel Sulfide Nanoframes from Metal-Organic Frameworks with Enhanced Pseudocapacitive and Electrocatalytic Properties. *Angew. Chemie* **2015**, *127* (18), 5421–5425.

(67) Yilmaz, G.; Tan, C. F.; Lim, Y. F.; Ho, G. W. Pseudomorphic Transformation of Interpenetrated Prussian Blue Analogs into Defective Nickel Iron Selenides for Enhanced Electrochemical and Photo-Electrochemical Water Splitting. *Adv. Energy Mater.* **2019**, *9* (1). 1802983.

(68) Yu, J.; Li, Q.; Li, Y.; Xu, C. Y.; Zhen, L.; Dravid, V. P.; Wu, J. Ternary Metal Phosphide with Triple-Layered Structure as a Low-Cost and Efficient Electrocatalyst for Bifunctional Water Splitting. *Adv. Funct. Mater.* **2016**, *26* (42), 7644–7651.

(69) Zhang, Y.; Gao, L.; Hensen, E. J. M.; Hofmann, J. P. Evaluating the Stability of Co_2P Electrocatalysts in the Hydrogen Evolution Reaction for Both Acidic and Alkaline Electrolytes. *ACS Energy Lett.* **2018**, *3* (6), 1360–1365.

(70) Friebel, D.; Louie, M. W.; Bajdich, M.; Sanwald, K. E.; Cai, Y.; Wise, A. M.; Cheng, M. J.; Sokaras, D.; Weng, T. C.; Alonso-Mori, R.; Davis, R. C.; Bargar, J. R.; Nørskov, J. K.; Nilsson, A.; Bell, A. T. Identification of Highly Active Fe Sites in (Ni,Fe)OOH for Electrocatalytic Water Splitting. *J. Am. Chem. Soc.* **2015**, *137* (3), 1305–1313.

(71) Su, H. Y.; Gorlin, Y.; Man, I. C.; Calle-Vallejo, F.; Norskov, J. K.; Jaramillo, T. F.; Rossmeisl, J. Identifying Active Surface Phases for Metal Oxide Electrocatalysts: A Study of Manganese Oxide Bi-Functional Catalysts for Oxygen Reduction and Water Oxidation Catalysis.

Phys. Chem. Chem. Phys. **2012**, *14* (40), 14010–14022.

(72) Zhang, G.; Wang, H.; Yang, J.; Zhao, Q.; Yang, L.; Tang, H.; Liu, C.; Chen, H.; Lin, Y.; Pan, F. Temperature Effect on Co-Based Catalysts in Oxygen Evolution Reaction. *Inorg. Chem.* **2018**, *57* (5), 2766–2772.

(73) Shinagawa, T.; Garcia-Esparza, A. T.; Takanabe, K. Insight on Tafel Slopes from a Microkinetic Analysis of Aqueous Electrocatalysis for Energy Conversion. *Sci. Rep.* **2015**, *5*, 13081.

(74) Roger, B. Y. The Rate of Electrolytic Hydrogen Evolution And the Heat of Adsorption of Hydrogen. *Trans. Faraday Soc.* **1958**, *54*, 1053–1063.

(75) Gong, M.; Zhou, W.; Tsai, M. C.; Zhou, J.; Guan, M.; Lin, M. C.; Zhang, B.; Hu, Y.; Wang, D. Y.; Yang, J.; Pennycook, S. J.; Hwang, B. J.; Dai, H. Nanoscale Nickel Oxide/Nickel Heterostructures for Active Hydrogen Evolution Electrocatalysis. *Nat. Commun.* **2014**, *5*, 4695.

(76) Ray, C.; Lee, S. C.; Jin, B.; Kundu, A.; Park, J. H.; Jun, S. C. Stacked Porous Iron-Doped Nickel Cobalt Phosphide Nanoparticle: An Efficient and Stable Water Splitting Electrocatalyst. *ACS Sustain. Chem. Eng.* **2018**, *6* (5), 6146–6156.

(77) Sultan, S.; Ha, M.; Kim, D. Y.; Tiwari, J. N.; Myung, C. W.; Meena, A.; Shin, T. J.; Chae, K. H.; Kim, K. S. Superb Water Splitting Activity of the Electrocatalyst $Fe_3Co(PO_4)_4$ Designed with Computation Aid. *Nat. Commun.* **2019**, *10* (1), 1–9.

BRIEFS

Self-supported NiFeP layer coated NiP rods are successfully fabricated by phosphidation of Prussian blue analogues grown on nickel phosphate rods. This core-shell electrocatalyst is

bifunctional, efficient and stable, enabling symmetric electrochemical water splitting in alkaline solution.

SYNOPSIS

TOC figure